# Effects of attenuation in single slow rotation dynamic SPECT

**T Humphries[1]‡, A Celler[2] and M Trummer[1]**

[1] Department of Mathematics, Simon Fraser University, 8888 University Ave, Burnaby, British Columbia, Canada, V5A 1S6

[2] Department of Radiology, University of British Columbia, 828 West 10th Avenue, Vancouver, British Columbia, Canada, V5Z 1L8

E-mail: thomash@sfu.ca, aceller@phas.ubc.ca

**Abstract.** Dynamic imaging using SPECT has been a topic of research interest for many years. Several proposed approaches have considered the reconstruction of dynamic images from SPECT data acquired with a conventional single slow rotation of the camera, which results in an extremely underdetermined reconstruction problem. Accurate attenuation correction (AC) is particularly important in this context, in order to distinguish the actual dynamic behaviour of the tracer within a region from the effects of attenuation on the projection data as the camera rotates around the patient. In this paper, we demonstrate that the standard approach to AC used in conventional SPECT imaging is not sufficient to account for the effects of attenuation in dynamic imaging of this type. As a result, artifacts may be created in the reconstructed images. Using realistic dynamic 3D phantom simulations, as well as real-life dynamic renal SPECT data, we assess the severity of these artifacts and investigate a method to eliminate them. The proposed method is shown to substantially improve the accuracy of the reconstructed image.

PACS numbers: 87.57.uh, 87.57.nf, 87.57cp

Submitted to: *Phys. Med. Biol.*

## 1. Introduction

Dynamic single photon emission computed tomography (SPECT) has the potential to provide valuable diagnostic information on *in vivo* dynamic processes, such as organ metabolism and/or blood flow. Dynamic SPECT has thus been a topic of considerable research interest over the last 15–20 years, as was recently highlighted in a comprehensive review article (Gullberg, Reutter, Sitek, Maltz & Budinger 2010). In this paper, we focus on single slow rotation dynamic SPECT, which aims to reconstruct a time series of 3D images from data acquired using a single conventional slow (e.g. 10–20 minute)

‡ Present address: Department of Mathematics, Memorial University of Newfoundland, St. John's, NL, Canada, A1C 5S7, P.O. Box 4200. thumphries@mun.ca

rotation of a SPECT camera. This approach has the advantage of not requiring specialized equipment, unlike many other proposed dynamic SPECT techniques that require cameras capable of performing multiple rotations at high speeds, on the order of 10–60 seconds per rotation (Smith, Gullberg, Christian & Datz 1994, Reutter, Gullberg & Huesman 2000, Kadrmas & Gullberg 2001). The signal-to-noise ratio of the projection data is also improved as a result of the slower rotation speed, although the data are highly inconsistent since the tracer distribution changes considerably during acquisition. Single slow-rotation approaches must therefore account for this inconsistency. For a thorough review of existing dynamic SPECT research, we refer readers to the aforementioned review article.

Single slow-rotation dynamic SPECT methods typically assume that the camera views a different distribution of activity at every stop, which results in a highly underdetermined reconstruction problem. Research has therefore focused on using temporal regularization techniques to eliminate physically unrealistic solutions, which may still fit the data well. One early approach modeled the time activity curve (TAC) in every voxel of the image as a sum of decaying exponentials (Limber, Limber, Celler, Barney & Borwein 1995). The dSPECT method, developed afterwards, uses linear inequalities to constrain the shape of the TAC in every voxel of the image (Farncombe, Celler, Noll, Maeght & Harrop 1999, Celler, Farncombe, Bever, Noll, Maeght, Harrop & Lyster 2000, Farncombe, Celler, Bever, Noll, Maeght & Harrop 2001, Humphries, Celler & Trummer 2011). A third proposed approach incorporates the method of factor analysis of dynamic systems (FADS) to model the dynamic activity in every voxel of the image as a linear combination of a small number of time-dependent factors (Sitek, Gullberg, Di Bella & Celler 2001).

Accurate attenuation correction (AC) is particularly important in single slow rotation dynamic SPECT, since otherwise the effects of attenuation on the projection data as the camera rotates are conflated with the actual dynamic behaviour of the tracer. Without AC it is not possible to determine, for instance, whether a reduction in the number of counts detected from a region is due to washout of the tracer, or due to an increase in attenuation between that region and the detector, caused by the rotation of the camera. Most single slow rotation dynamic SPECT studies have thus included the attenuation map in the system matrix used for image reconstruction, as is done in conventional SPECT imaging. In this paper, we demonstrate that, as a consequence of the highly underdetermined nature of slow-rotation dynamic SPECT image reconstruction, this approach is not always sufficient to properly compensate for attenuation effects. We illustrate this fact using digital phantom simulations, as well as real data corresponding to two dynamic renal scans. We also show that beginning the reconstruction from a more accurate initial estimate may successfully reduce or eliminate artifacts that arise due to this issue.

## 2. Problem description

The system model for static SPECT imaging is given by

$$\mathbf{C}\mathbf{x} = \mathbf{p}, \tag{1}$$

where $\mathbf{x}$ is the image vector representing the distribution of activity, $\mathbf{p}$ is the vector of binned projection data, and $\mathbf{C}$ is the system matrix modeling the propagation and detection of photons emitted by the activity, with element $\mathbf{C}_{ji}$ representing the contribution of the $i$th image voxel to the $j$th bin. The unknown image $\mathbf{x}$ can then be estimated using an iterative method such as maximum likelihood expectation maximization (MLEM) (Shepp & Vardi 1982):

$$\mathbf{x}_i^{(n+1)} = \frac{\mathbf{x}_i^{(n)}}{\sum_j \mathbf{C}_{ji}} \sum_j \mathbf{C}_{ji} \frac{\mathbf{p}_j}{\sum_{i'} \mathbf{C}_{ji'} \mathbf{x}_{i'}^{(n)}}, \tag{2}$$

where $\mathbf{x}_i^{(n)}$ is the activity estimate in voxel $i$ after $n$ iterations. The initial estimate $\mathbf{x}^{(0)}$ is often chosen to be a uniform vector where every element is equal to one.

In single slow rotation dynamic SPECT, this system model is modified. The size of $\mathbf{p}$ does not change, but the dynamic image vector, which we denote as $\mathbf{x}'$, is enlarged by a factor of $K$, where $K$ is the number of time frames in the image (usually assumed to be equal to the number of stops made by the camera). The system matrix, denoted $\mathbf{C}'$, therefore has $K$ times as many columns as well. This matrix is in fact just a reordering of $\mathbf{C}$ into a block-diagonal form, since the camera geometry is the same as in the static case, and the activity distribution at time $k$ only contributes to the $k$th projection.

In the dSPECT algorithm, which we use in this paper, the EM-based update formula is given by:

$$\tilde{\mathbf{x}}_{i,k}^{(n+1)} = \frac{\tilde{\mathbf{x}}_{i,k}^{(n)}}{\sum_j \left(\mathbf{C}'_{ji,k} \mathbf{A}_{i,k}^{-1}\right)} \sum_j \mathbf{C}'_{ji,k} \mathbf{A}_{i,k}^{-1} \frac{\mathbf{p}_{j,k}}{\sum_{i'} \mathbf{C}'_{ji',k} \mathbf{A}_{i',k}^{-1} \tilde{\mathbf{x}}_{i',k}^{(n)}}, \tag{3}$$

where $\mathbf{A}$ is a matrix which constrains the shape of the TAC in every voxel of the image. Essentially, dSPECT restricts the solution by making a change of variable from $\mathbf{x}'$ to the vector $\tilde{\mathbf{x}} = \mathbf{A}\mathbf{x}'$, and then optimizing over $\tilde{\mathbf{x}}$. As a result of this change of variable, the TAC in any voxel of the image $\mathbf{x}'$ is constrained by the mapping $\mathbf{A}^{-1}$ to one of three behaviours: increasing, decreasing, or increasing to a peak value and then decreasing. Since it may not be known *a priori* which of these constraints is appropriate, the assumed behaviour for each voxel can be adjusted between iterations of the algorithm, to better fit the data. More details on the algorithm are presented in (Farncombe et al. 2001).

In static iterative SPECT reconstruction, attenuation correction (AC) is achieved by incorporating the attenuation map into the matrix $\mathbf{C}$. Doing this allows the algorithm to properly model the effects of attenuation and thus converge to an accurate image. Even so, AC may be less effective in some regions of the image than in others (Hutton, Nuyts & Zaidi 2006). A simple 2D phantom simulation presented in Figure 1 provides an illustration. When data were acquired over 360° and AC was performed (right

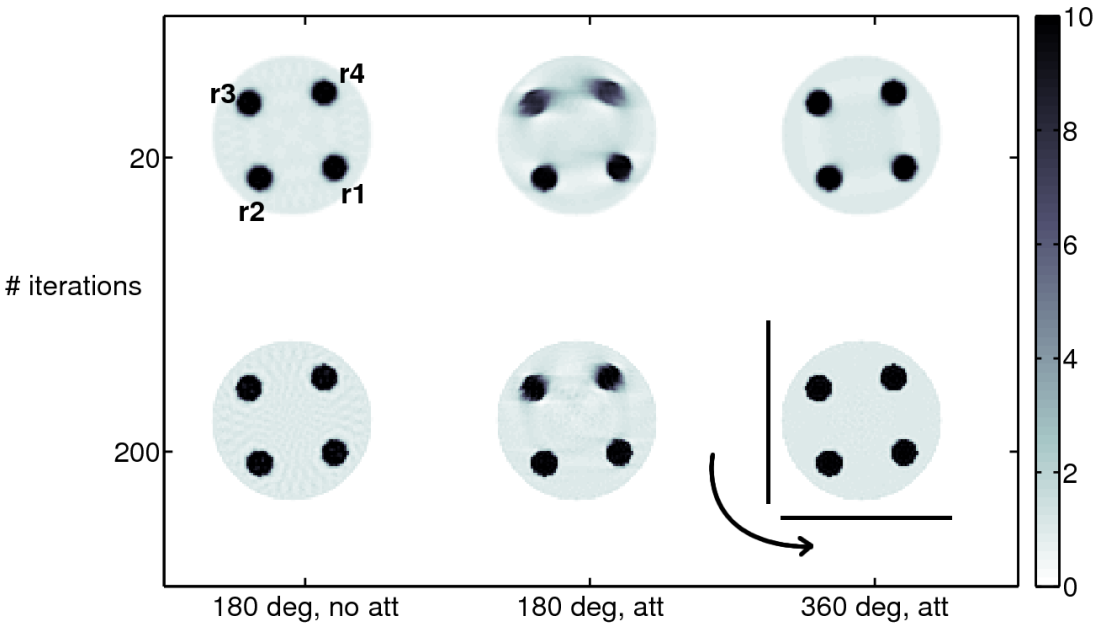


**Figure 1.** Simulation consisting of static images reconstructed after 20 and 200 iterations of MLEM. Reconstructed images in centre and right columns included attenuation with $\mu = 0.15$ cm$^{-1}$ within the object. Projection data consisted of 32 views over the bottom 180° arc for the left and middle columns, and 64 views over 360° for the right column. No noise or collimator blurring were included in the projection data. Image in the bottom right corner shows the initial position of camera detectors and direction of rotation for the dynamic phantom simulation (shown in Figure 2).

column), the reconstruction converged relatively quickly, with no apparent artifacts due to attenuation visible after 20 iterations of MLEM. This is evident from comparing against the image in the left column, where the effects of attenuation were not included in the simulation. When data were acquired over a 180° arc, however (middle column), regions on the opposite side of the object (labeled r3 and r4) were badly distorted after the same number of iterations. The algorithm eventually converged to an accurate image where these distortions were largely eliminated, but only after many iterations (bottom row, middle column). The key point is that AC did not instantly compensate for the fact that counts from r3 and r4 were more attenuated than counts from other regions. The effectiveness of AC depends to some extent on the completeness of the available projection data.

We now consider a second phantom simulation which illustrates how a similar effect can produce artifacts in slow rotation dynamic SPECT images. This simulation used the same geometry as the static example, but featured dynamic activity in each of the four small regions. All four regions were assigned the same dynamic behaviour, modeling uptake and washout of a tracer over 20 minutes. A dual-head, 90° mode acquisition was

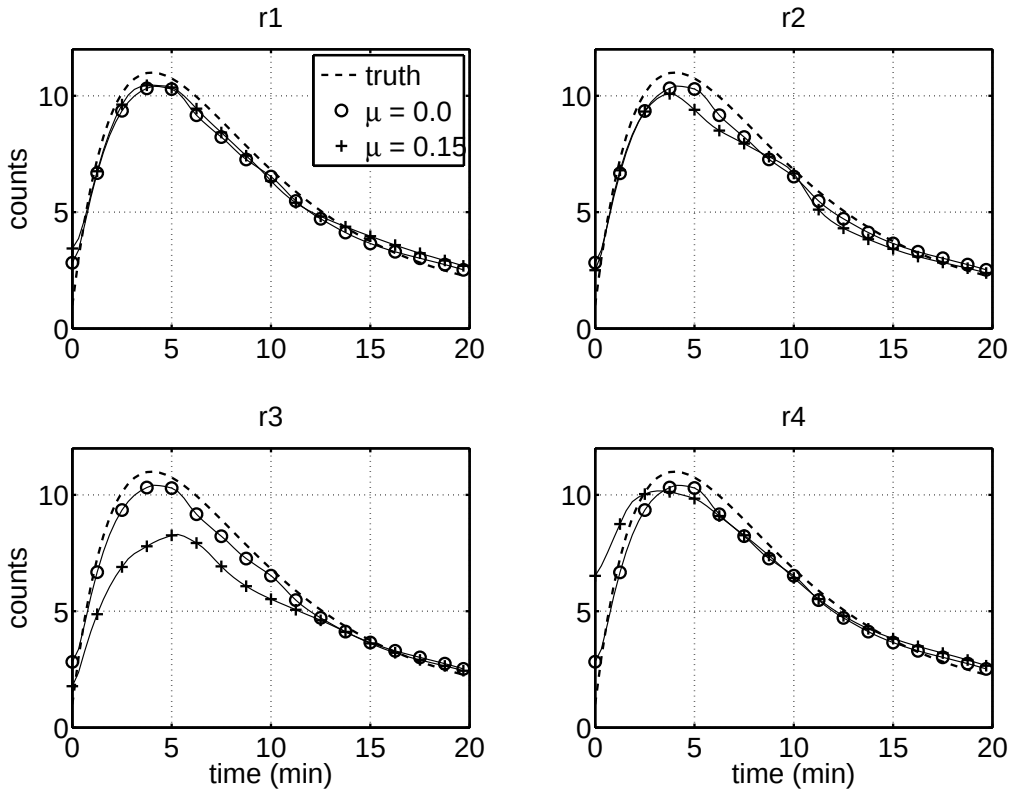


**Figure 2.** Mean TACs extracted from each of the four dynamic regions r1–r4. Dashed line shows true TAC; line with circular markers, the TAC extracted from the attenuation-free reconstructed image; and line with cross markers, the TAC extracted from the reconstructed image including attenuation effects.

simulated, where each head made 64 stops over a 360° rotation, as shown in the bottom right-hand corner of Figure 1. Two sets of projection data were created: one without attenuation, and one assuming uniform attenuation of $\mu = 0.15$ cm$^{-1}$ inside the object. The two corresponding images were then reconstructed using 80 iterations of dSPECT with the appropriate system matrix (i.e. with or without AC). The simulation without attenuation provided a baseline for how accurate an image we could expect, given perfect AC. Additionally, since the kinetic behaviour in each of the four regions was identical, any discrepancies between the reconstructed TACs in the second simulation must have occurred due to the differing effects of attenuation on each region. Noise and collimator blurring were not included in the projection data.

The mean TACs extracted from the four dynamic regions are shown in Figure 2. The TACs for the attenuation-free image (circular markers) are the same in all four regions, but the TACs for the image with attenuation (cross markers) are not. In particular, the TAC in r3 is severely underestimated, and smaller discrepancies are also visible in the TACs for r2 and r4. The TAC in r1, on the other hand, is essentially identical to the TAC reconstructed in the simulation without attenuation. These

discrepancies occur due to the conflation of attenuation effects caused by the camera rotation with the actual tracer dynamics. In the simulated acquisition, the detectors started on the bottom and left sides of the object and rotated counterclockwise. Thus, at least one detector remained close to r1 throughout the first 10 minutes – when the activity was changing most rapidly – and so the effect of attenuation on the TAC in this region was negligible. Meanwhile, because the detectors rotated away from r3 during these first 10 minutes, the amount of attenuating material between this region and the detectors increased during this time period, resulting in an underestimation of the actual activity present in this region.

A key difference from the static simulation presented earlier is that these artifacts were not eliminated even after hundreds of iterations of dSPECT. This is due to the highly underdetermined nature of the single slow rotation dynamic SPECT reconstruction problem. As a result of this underdeterminacy, incorrect solutions such as the one shown in Figure 2 may fit the projection data just as well as solutions which more accurately represent the dynamic behaviour. In other words, modeling attenuation in the system matrix is necessary, but not sufficient to ensure that dSPECT converges to an accurate image. It is interesting that this effect has not been noted in previous studies on single slow rotation dynamic SPECT. This is likely due to the fact that many of these studies featured simulations involving centrally-located dynamic objects as well as triple-head cameras, which would reduce the disparity in attenuation effects on different regions of the object. Any artifacts that were noticed may also have simply been attributed to the difficulty of the reconstruction problem, without realizing that they were specifically related to attenuation. We note as well that collimator blurring correction is similarly affected in the context of single slow rotation dynamic SPECT, although artifacts in this case are of course much smaller than those caused by attenuation.

A straightforward technique which may reduce or eliminate these artifacts is to begin reconstruction from a better initial estimate. The reconstructed image shown in Figure 2 was produced by dSPECT after starting with a uniform initial estimate, as is common practice when using iterative reconstruction algorithms. As a result, dSPECT converged to a local minimum; i.e., an image that fits the data, but contains attenuation artifacts. Starting from a better initial estimate could allow dSPECT to avoid this local minimum and converge to a more accurate image. In this paper, we propose the following procedure, which we denote as the "template IE" (initial estimate) method:

(i) A dynamic image $\mathbf{x}'$ is first reconstructed from a uniform initial estimate ("uniform IE") using dSPECT. The resulting image may contain attenuation artifacts.

(ii) This image is segmented into regions of interest (ROIs) that are assumed to have consistent dynamic behaviour. The segmentation could be created based on prior anatomical knowledge, or simply by examining the image resulting from Step 1.

(iii) A dynamic digital template, denoted $\mathbf{y}'$, is created by averaging the TACs over all

**Table 1.** Description of the dynamic behaviour in each kidney for the six renal phantom simulations. In simulations E and F, unhealthy behaviour was assigned only to voxels in the inferior one-third of one kidney, while the remaining voxels in the upper part of that kidney were assigned healthy behaviour.

| Case | Left kidney | Right kidney | Case | Left kidney | Right kidney |
|---|---|---|---|---|---|
| A | healthy | healthy | D | healthy | unhealthy |
| B | unhealthy | unhealthy | E | $\frac{1}{3}$ unhealthy | healthy |
| C | unhealthy | healthy | F | healthy | $\frac{1}{3}$ unhealthy |

voxels in each ROI. In other words, $\mathbf{y}'$ is a smoothed approximation to $\mathbf{x}'$, where every voxel in every ROI is assigned the average TAC for that ROI.

(iv) This template is used as the initial estimate in a second run of dSPECT. This second run may require fewer iterations to converge than the first.

## 3. Experiments

In the simulation shown in Figure 2, the most severe artifacts occurred in r3 and r4. In a real-life study, artifacts are not likely to be this severe, since the acquisition would be chosen such that the camera heads remain as close as possible to the regions being imaged – particularly during the early part of the scan, when the dynamic behaviour is likely to be most rapid. In this section, we investigate the more realistic scenario of dynamic renal SPECT imaging. Several dynamic 3D digital phantom simulations, as well as two images reconstructed from real-life dynamic renal SPECT scans, are examined to assess the severity of any artifacts arising as a result of the conflation of attenuation with dynamic behaviour, as well as the effectiveness of the template IE method in reducing these artifacts.

### *3.1. Dynamic 3D renal phantom simulations*

To create a digital dynamic renal phantom, a 64×64×64 voxel anatomical map (voxel size 9.3mm/side) was first created using the 3D NCAT digital phantom (Segars, Lalush & Tsui 1999). This map provided region boundaries corresponding to the torso, kidneys, ureters, and bladder. Tracer kinetics modeling the uptake and washout of $^{99m}$Tc-DTPA in the renal system were simulated using a kinetic model. This model has been used in a previous dSPECT study (Humphries, Saad, Celler, Hamarneh, Möller & Trummer 2009), and is described in detail in that paper. Two types of renal behaviour, healthy and unhealthy, were modeled. Healthy behaviour was modeled as uptake of the tracer in the kidney followed by fairly rapid washout (effective half-life $T_{\frac{1}{2}}$ of 290 seconds), while washout in the unhealthy case was much slower ($T_{\frac{1}{2}} = 2135$ s). Six different phantoms (denoted A–F) were simulated using different combinations of healthy and unhealthy behaviour in either kidney, as summarized in Table 1.

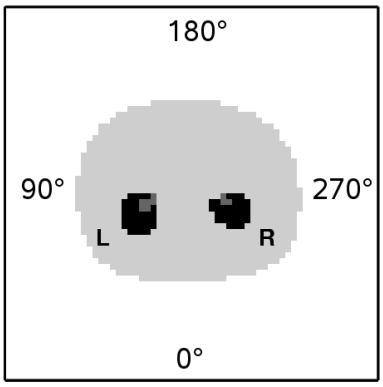


**Figure 3.** Transaxial slice through the dynamic renal phantom, showing background region, kidneys, and ureters. Angular convention is used to describe acquisitions in Table 2. Left and right kidneys are indicated by "L" and "R".

Two experiments were run using the digital phantom. In both experiments, projection data of the phantom were generated analytically, with Poisson noise added to the data afterwards, in proportion to the total counts. For the simulated count rate in these experiments, this corresponded to a noise level of roughly 5–7%. In the first experiment, four different acquisition protocols were simulated for each of the phantoms A–D, for a total of sixteen simulations. The four acquisitions, which were numbered I–IV, all featured two detectors at 90° to one another, each of which rotated 360°, making 48 stops lasting 20 seconds each. The two parameters that were varied were the initial position of the detectors and the direction of rotation. All four acquisitions were chosen sensibly so that the camera acquired data posteriorly during the early part of the scan. The parameters for each of these acquisitions are given in Table 2. Dynamic images based on these data were reconstructed using 60 iterations of dSPECT, beginning from a uniform IE. Mean TACs were then extracted from the left and right kidneys, by averaging over all voxels contained within the true organ boundaries. A measure of relative error in the mean TAC for each kidney was computed as:

$$\varepsilon = \left\|\tau - \tau^{\text{true}}\right\|_2 \Big/ \left\|\tau^{\text{true}}\right\|_2 \times 100\%, \tag{4}$$

where $\tau$ is the $1 \times 48$ vector representing the mean TAC obtained from the reconstructed image, and $\tau^{\text{true}}$ the equivalent vector representing the true TAC. These values were compared across simulations to assess the effect of the acquisition protocol on the accuracy of the mean TAC in each kidney. Any bias introduced by the acquisition protocol towards either kidney is concerning, since renal split function (i.e. the proportion of total renal function attributed to each of the kidneys) is often a quantity of interest in renal studies.

In the second experiment, Acquisition II was used to generate projection data corresponding to all six phantoms A–F. We then applied the template IE method to

**Table 2.** Parameters used in the four simulated acquisitions I–IV. The angular conventions used to indicate initial position of heads are shown in Figure 3. "cw" and "ccw" refer to clockwise and counterclockwise rotations, respectively.

| Acquisition | I | II | III | IV |
|---|---|---|---|---|
| Initial pos. | 135° + 45° | 90° + 0° | 270° + 0° | 225° +315° |
| Rotation | 360° ccw | 360° ccw | 360° cw | 360° cw |

the reconstruction. The true organ boundaries were used to create the template $\mathbf{y}'$, and only 40 iterations were used in the second run of dSPECT. The error measures $\varepsilon$ were computed for the resulting images and compared against the values for the original (uniform IE) image $\mathbf{x}'$. For Phantoms E and F, two situations were considered; one where the unhealthy portion of the kidney was correctly segmented during the creation of the template, and one where it was incorrectly included in a segment corresponding to the entire kidney. The goal was to assess how much the effectiveness of the method suffered in this second case.

### *3.2. Volunteer renal data experiment*

Dynamic renal scans (370 MBq $^{99m}$Tc-DTPA) of two consenting adult volunteers were acquired using a dual-head Siemens Symbia T2 SPECT/CT system, with detectors positioned at 90°, and AC data provided by the 2 slice CT scanner. A planar renogram of both volunteers, taken two days prior to the SPECT scan, indicated that both had healthy renal function. During the SPECT acquisition, the camera heads started on the posterior and left sides of each volunteer, and completed a 360° rotation consisting of 64 stops of 20 seconds each. Images consisting of 128 × 128-voxel slices (voxel size 4.79 mm) and sixty-four time frames were reconstructed using 60 iterations of dSPECT, beginning from a uniform IE. The template IE method was then applied to produce a second image.

When creating the template to produce this second image, we had to take into consideration that the renal pelves (the central part of each kidney) showed noticeably delayed uptake and higher peak activity concentration compared to the the renal cortices (outer part of each kidney), as is typical for renal imaging agents. Thus, the cortex and pelvis of each kidney had to be considered as distinct dynamic regions during the creation of the template. Segmentation was performed by examining the simultaneously acquired CT image slice-by-slice to identify the left and right kidneys, while the renal pelvis in each kidney was identified by examining slices of the reconstructed image that had been summed over time.

Since there was no known truth against which to compare the images generated in this experiment, it was not possible to compute the error measure $\varepsilon$ and establish with certainty whether the the template IE method produced more accurate TACs than the uniform IE image. Instead, we compared the images reconstructed from a uniform IE

**Table 3.** Average $\varepsilon$ (%) values taken over the four acquisitions for each phantom (left half of the table) and over the four phantoms for each acquisition (right half of the table). LK and RK refer to errors in the left and right kidneys, respectively.

| | Average value | | | Average value | |
|---|---|---|---|---|---|
| Phantom | LK | RK | Acquisition | LK | RK |
| A | 18.8 | 19.3 | I | 14.4 | 19.5 |
| B | 15.6 | 16.5 | II | 18.4 | 16.5 |
| C | 15.4 | 20.4 | III | 16.4 | 21.9 |
| D | 18.9 | 16.7 | IV | 19.6 | 15.1 |

and from the template IE, to see if the effects of the template IE method were similar to those observed in the phantom experiments. We first compared the relative difference in reconstructed peak activity between the two images, for both the left and right kidney cortices. These quantities were denoted LK+ and RK+, respectively. Within each image, we also computed the relative difference between the peak activities in the left and right kidneys, denoted by $\Delta_{RL}$. The formulas for these measures are given by:

$$\begin{aligned} \text{LK+} &= (\tau^{\max}_{\text{LK, tmpl}} - \tau^{\max}_{\text{LK, unif}}) \Big/ \tau^{\max}_{\text{LK, unif}} \times 100\%, \\ \text{RK+} &= (\tau^{\max}_{\text{RK, tmpl}} - \tau^{\max}_{\text{RK, unif}}) \Big/ \tau^{\max}_{\text{RK, unif}} \times 100\%, \\ \Delta_{RL} &= (\tau^{\max}_{\text{RK}} - \tau^{\max}_{\text{LK}}) \Big/ \tau^{\max}_{\text{LK}} \times 100\%, \end{aligned} \tag{5}$$

where $\tau^{\max}_{\text{LK, unif}}$ refers to the peak activity in the left kidney of the image reconstructed from a uniform initial estimate, $\tau^{\max}_{\text{LK, tmpl}}$ to the peak activity in the left kidney of the image reconstructed using the template IE method, and correspondingly for the other quantities. Since both volunteers had healthy renal function, a large $\Delta_{RL}$ value could indicate that activity in one of the kidneys was being underestimated relative to the other. The purpose of computing RK+ and LK+ was to see if the template IE method compensated for any such errors by scaling the counts in either kidney appropriately.

## 4. Results

The $\varepsilon$ values from the first phantom simulation experiment are summarized in Table 3. The results of the phantom experiment where the template IE approach was applied are shown in Table 4 (Phantoms A–D) and Table 5 (Phantoms E–F). The LK+, RK+ and $\Delta_{RL}$ values for the volunteer renal scan experiment are tabulated in Table 6.

**Table 4.** Error values $\varepsilon$ (%) for images reconstructed with and without the template IE method, for Phantoms A–D.

| | Uniform IE | | Template IE | |
|---|---|---|---|---|
| Phantom | LK | RK | LK | RK |
| A | 20.5 | 15.6 | 4.2 | 4.5 |
| B | 15.7 | 16.4 | 2.1 | 4.0 |
| C | 15.9 | 17.1 | 2.3 | 5.0 |
| D | 21.5 | 16.8 | 4.5 | 4.1 |
| Average | 18.4 | 16.5 | 3.3 | 4.4 |

**Table 5.** Error values $\varepsilon$ (%) for images reconstructed with and without the template IE method, for Phantoms E and F. "LKu/RKu" refer to the unhealthy portion of the left or right kidney (bottom $\frac{1}{3}$), while "LKh/RKh" refer to the healthy portion (the remainder of that kidney). The first row of data refers only to the image reconstructed from a uniform IE, while the last two rows refer to images reconstructed using the template IE method with the correct and incorrect segmentations, respectively.

| | Phantom E | | | | | | Phantom F | | | | | |
|---|---|---|---|---|---|---|---|---|---|---|---|---|
| | Uniform IE | | | Template IE | | | Uniform IE | | | Template IE | | |
| Segmentation | LKu | LKh | RK | LKu | LKh | RK | LK | RKu | RKh | LK | RKu | RKh |
| None | 18.4 | 22.7 | 15.1 | — | — | — | 19.3 | 18.8 | 21.7 | — | — | — |
| Correct | — | — | — | 2.1 | 3.3 | 5.9 | — | — | — | 4.3 | 4.2 | 8.3 |
| Incorrect | — | — | — | 2.9 | 7.8 | 5.9 | — | — | — | 4.3 | 6.8 | 15.6 |

**Table 6.** Effect of the template IE method on the mean TACs of the images reconstructed from the two sets of volunteer renal data.

| | Uniform IE | Template IE | | |
|---|---|---|---|---|
| | $\Delta_{RL}$ | LK+ | RK+ | $\Delta_{RL}$ |
| Volunteer #1 | 12.1 | 30.0 | 27.3 | 9.8 |
| Volunteer #2 | 11.4 | 39.2 | 28.8 | 3.1 |

## 5. Discussion

### *5.1. Phantom simulations*

Several trends are apparent from the data presented in the left half of Table 3. When averaged over all acquisitions, the errors in the right kidney tended to be larger than errors in the left kidney, possibly since the right kidney was approximately 10% smaller than the left kidney in the phantom geometry, making it more challenging to reconstruct accurately. Also, the value of $\varepsilon$ when a kidney featured healthy behaviour (fast washout)

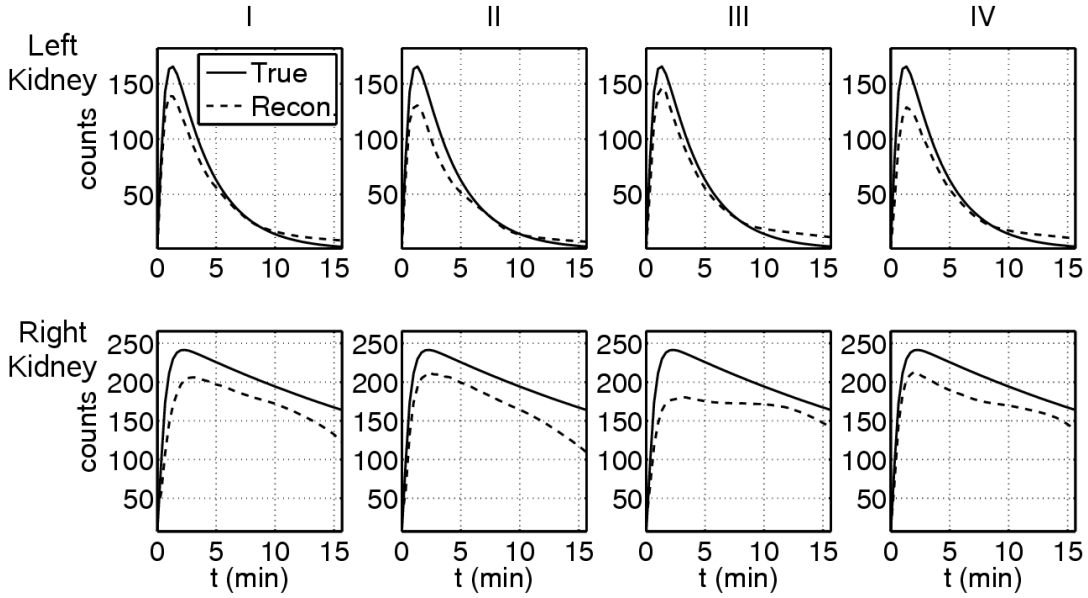


**Figure 4.** Mean TACs (dashed lines) extracted from reconstructed images of Phantom D, starting from a uniform IE. True TAC shown as a solid line in each plot. Columns correspond to acquisition protocols used to acquire the data.

was typically larger than when a kidney featured unhealthy behaviour (slow washout), since the relative underestimation of the TAC was greater, particularly at the point of maximum activity. This was not surprising, as rapid kinetic behaviour is generally more difficult to reconstruct accurately than gradual behaviour. Taking these factors into account, it is evident from the right half of the table that each of the four acquisition protocols tended to reconstruct the TAC in one kidney more accurately than in the other. Specifically, Acquisitions I and III both consistently gave less accurate results for the right kidney than for the left kidney, while the opposite was true of Acquisitions II and IV.

The results of this experiment are consistent with the effects observed in the 2D dynamic simulation described in Section 2. Specifically, the accuracy of the reconstructed TAC in either kidney was affected by changes in the amount of attenuating material between that kidney and the detectors as the camera rotated. For instance, in Acquisition III, the heads rotated away from the right kidney and towards the left kidney during the first four minutes of the acquisition. As a result, the TAC in the right kidney was underestimated relative to the TAC in the left kidney during this time period. Figure 4 shows an example of how the accuracy of the reconstructed mean TACs was affected by the acquisition protocol, for one of the simulated phantoms.

The results of the second experiment (Tables 4 and 5) show that $\varepsilon$ was substantially reduced by the application of the template IE method in all cases. Figure 5 shows the mean TACs in the left and right kidneys for the simulation of Phantom C, before and after the application of this method. It is apparent from this figure that starting from the more accurate initial estimate has improved the accuracy of the mean TACs and

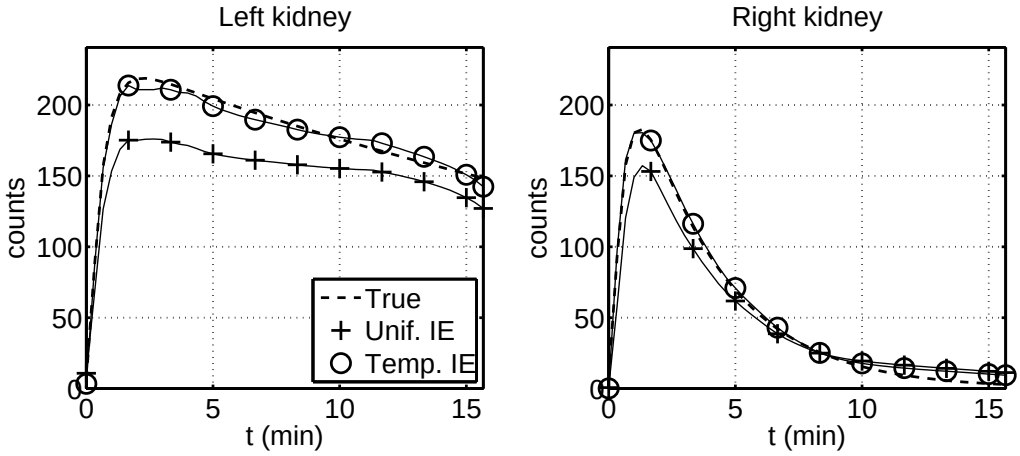


**Figure 5.** Mean TACs extracted from the left and right kidney ROIs of the reconstructed image of Phantom C. Dashed line in each plot represents the true TAC, cross markers the TAC corresponding to the image reconstructed from a uniform IE, and circular markers the TAC corresponding to the image reconstructed from the template IE.

compensated for attenuation artifacts present in the uncorrected image. For instance, the left kidney TAC in the uniform IE image was more severely underestimated during the first eight minutes than during the last eight minutes, since the camera heads in Acquisition II initially rotated away from the left kidney. In the image produced using the template IE method, this discrepancy has been eliminated.

The results for phantom simulations E and F are presented in Table 5. When the correct segmentation was used, the reduction in $\varepsilon$ was on par with that obtained for the simulations using Phantoms A–D. When the incorrect segmentation was used, the template was inaccurate since both regions of the partially unhealthy kidney were assigned a single TAC that was a combination of the healthy and unhealthy behaviours. This error in segmenting the image resulted in mean TAC errors $\varepsilon$ for these regions that were roughly twice as large compared to when the correct segmentation was used. These $\varepsilon$ values were still smaller than those in the uniform IE image, however, indicating that the application of the template IE method with an incorrect segmentation did not worsen the accuracy of the image, and in fact still provided some compensation for the effects of attenuation on the image.

### *5.2. Volunteer data*

The acquisition protocol used to acquire the volunteer data was analogous to Acquisition II in the phantom simulations. Thus, we expected that the TAC in the left kidney of the reconstructed images would be underestimated compared to the TAC in the right kidney. The results of this experiment suggest that the same attenuation effect that we observed in the phantom simulations was indeed present. Table 6 shows that the value of LK+ was greater than RK+ in both volunteer images, indicating that using

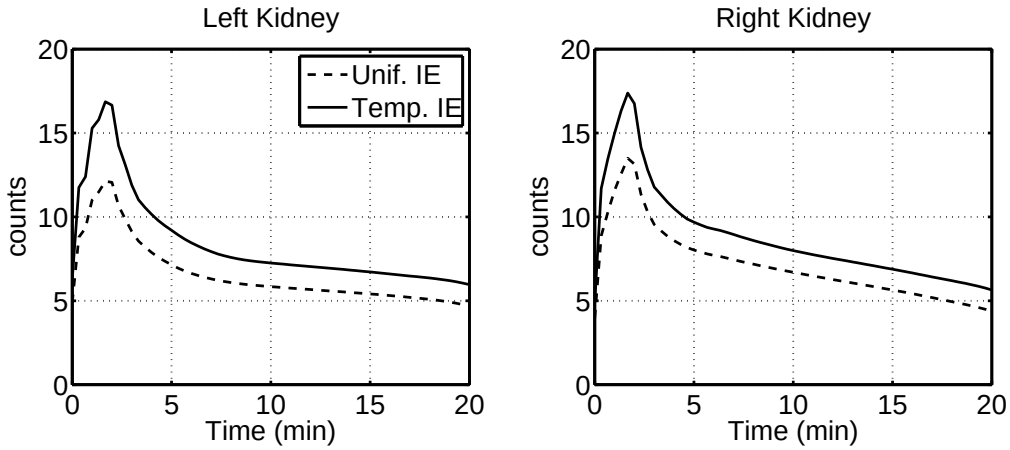


**Figure 6.** Mean TACs extracted from left and right kidney regions of reconstructed images of Volunteer #2. Dashed line corresponds to the TAC from the image reconstructed from a uniform IE, and solid line to the TAC from the image reconstructed from the template IE.

the template IE method raised the amount of activity reconstructed in the left kidney by a greater degree than the activity in the right kidney. This suggests that the counts in the left kidney were underestimated. Applying this method also reduced $\Delta_{RL}$, the discrepancy in peak activities between the left and right kidneys, in both cases. Since the planar scan of both volunteers indicated that the split function was roughly equal, a reduction in $\Delta_{RL}$ indicates that the reconstruction accuracy was probably improved. Figure 6 shows average TACs in each kidney from the reconstructed image of Volunteer #2, where the reduction of this discrepancy was most apparent.

## 6. Conclusions

In this paper, we have shown that in single slow-rotation dynamic SPECT imaging, the conventional approach to attenuation correction is insufficient, due to the highly underdetermined nature of the reconstruction problem. While we have used only the dSPECT algorithm in the paper, this finding should also be applicable to other methods which attempt to reconstruct dynamic images from such data. Although the severity of these artifacts may differ depending on the choice of reconstruction algorithm and the nature of the temporal regularization imposed on the reconstruction, the artifacts themselves occur strictly as a result of the limited nature of the projection data.

In dynamic 3D phantom simulations of a renal SPECT study, it was shown that when images were reconstructed beginning from a uniform initial estimate, the accuracy of the reconstructed TAC corresponding to either kidney varied depending on the protocol used to acquire the data, due to conflation of attenuation with dynamic behaviour. Experiments using volunteer renal data suggested that the same effects were present in real-life scans. The template IE method, which starts the reconstruction from a more accurate initial estimate, was found to substantially improve the accuracy of the

mean TACs in the phantom simulations, and to provide correction for the differing effects of attenuation on either kidney. In the experiments with real-life renal data, the effect of this method on the reconstructed mean TAC in either kidney was shown to be similar to that observed in the phantom simulations. We note that beginning an iterative algorithm from a better initial estimate is a general technique, which could provide benefits in other underdetermined image reconstruction problems as well.

At the present time, there is a great deal of interest in performing dynamic SPECT imaging using newer-model SPECT systems, which acquire multiple views of the patient simultaneously using detectors arranged in a stationary or quasi-stationary manner (Gambhir, Berman, Ziffer, Nagler, Sandler, Patton, Hutton, Sharir, Ben Haim & Ben Haim 2009, Slomka, Berman & Germano 2010, Buechel, Herzog, Husmann, Burger, Pazhenkottil, Treyer, Valenta, von Schulthess, Nkoulou, Wyss & Kaufmann 2010). Dynamic images produced using these systems should be largely free of the artifacts discussed in this paper, since these systems acquire data from all angles simultaneously. We note that, although it is possible to produce dynamic images with these systems by using a conventional algorithm such as OSEM to reconstruct each time frame independently, integrated 4D reconstruction approaches such as dSPECT may still be preferable due to the temporal regularization techniques that they employ.

## Acknowledgments

We thank Dr. Troy Farncombe for providing the dSPECT software, as well as for his advice and consultation. We thank the personnel at St. Paul's Hospital, Vancouver, British Columbia, for their assistance in acquiring the volunteer patient data, particularly Dr. Rajpaul Attariwala, Dr. George Sexsmith and Nazma Tarmohamed. Volunteer data were acquired following approval from the Clinical Research Ethics Board of the University of British Columbia. The authors acknowledge support from the Natural Sciences and Engineering Research Council of Canada.

## References

Buechel, R., Herzog, B., Husmann, L., Burger, I., Pazhenkottil, A., Treyer, V., Valenta, I., von Schulthess, P., Nkoulou, R., Wyss, C. & Kaufmann, P. (2010). Ultrafast nuclear myocardial perfusion imaging on a new gamma camera with semiconductor detector technique: first clinical validation, *European Journal of Nuclear Medicine and Molecular Imaging* **37**: 773–778.

Celler, A., Farncombe, T., Bever, C., Noll, D., Maeght, J., Harrop, R. & Lyster, D. (2000). Performance of the dynamic single photon emission computed tomography (dSPECT) method for decreasing or increasing activity changes, *Phys. Med. Biol.* **45**(12): 3525–3543.

Farncombe, T., Celler, A., Bever, C., Noll, D., Maeght, J. & Harrop, R. (2001). The incorporation of organ uptake into dynamic SPECT (dSPECT) image reconstruction, *IEEE Trans. Nucl. Sci.* **48**(1): 3–9.

Farncombe, T., Celler, A., Noll, D., Maeght, J. & Harrop, R. (1999). Dynamic SPECT imaging using a single camera rotation (dSPECT), *IEEE Trans. Nucl. Sci.* **46**(4): 1055–1061.

Gambhir, S., Berman, D., Ziffer, J., Nagler, M., Sandler, M., Patton, J., Hutton, B., Sharir, T.,

Ben Haim, S. & Ben Haim, S. (2009). A novel high-sensitivity rapid-acquisition single-photon cardiac imaging camera, *J. Nucl. Med.* **50**(4): 635–643.

Gullberg, G. T., Reutter, B. W., Sitek, A., Maltz, J. S. & Budinger, T. (2010). Dynamic single photon emission computed tomography – basic principles and cardiac applications, *Phys. Med. Biol.* **55**(20): R111–R191.

Humphries, T., Celler, A. & Trummer, M. (2011). Slow-rotation dynamic SPECT with a temporal second derivative constraint, *Medical Physics* **38**(8).

Humphries, T., Saad, A., Celler, A., Hamarneh, G., Möller, T. & Trummer, M. (2009). Segmentation-based regularization of dynamic SPECT reconstruction, *IEEE Nuclear Science Symposium Conference Record 2009*, pp. 2849–2852.

Hutton, B., Nuyts, J. & Zaidi, H. (2006). *Quantitative analysis in Nuclear Medicine Imaging; Chapter 4 – Iterative Reconstruction Methods*, Springer.

Kadrmas, D. J. & Gullberg, G. (2001). 4D maximum a posteriori reconstruction in dynamic SPECT using a compartmental model-based prior, *Phys. Med. Biol.* **46**(5): 1553–1574.

Limber, M., Limber, M., Celler, A., Barney, J. & Borwein, J. (1995). Direct reconstruction of functional parameters for dynamic SPECT, *IEEE Trans. Nucl. Sci.* **42**: 1249–1256.

Reutter, B., Gullberg, G. & Huesman, R. (2000). Direct least-squares estimation of spatiotemporal distributions from dynamic SPECT projections using a spatial segmentation and temporal B-splines, *IEEE Trans Med. Imag.* **19**: 434–450.

Segars, W., Lalush, D. & Tsui, B. (1999). A realistic spline-based dynamic heart phantom, *IEEE Trans. Nucl, Sci.* **46**(3): 503–506.

Shepp, L. & Vardi, Y. (1982). Maximum likelihood reconstruction for emission tomography, *IEEE Trans. Med. Imag.* **MI-2**: 113–122.

Sitek, A., Gullberg, G., Di Bella, E. & Celler, A. (2001). Reconstruction of dynamic renal tomographic data acquired by slow rotation, *J. Nucl. Med.* **42**: 1704–1712.

Slomka, P., Berman, D. & Germano, G. (2010). New imaging protocols for new single photon emission CT technologies, *Current Cardiovascular Imaging Reports* **3**(3): 162–170.

Smith, A., Gullberg, G., Christian, P. & Datz, F. (1994). Kinetic modeling of teboroxime using dynamic SPECT imaging of a canine model, *J. Nucl. Med.* **35**(3): 484–495.